

Combustion for aerospace propulsion

Eulerian and Lagrangian Large-Eddy Simulations of an evaporating two-phase flow

J.M. Senoner^{a,*}, M. Sanjosé^a, T. Lederlin^b, F. Jaegle^a, M. García^a, E. Riber^a,
B. Cuenot^a, L. Gicquel^a, H. Pitsch^b, T. Poinso^c

^a Cerfacs, 42, avenue Gaspard-Coriolis, 31057 Toulouse cedex 01, France

^b Center for Turbulence Research, 488 Escondido Mall, Stanford, CA 94305-3035, USA

^c Institut de mécanique des fluides de Toulouse (CNRS-INPT-UPS), allée du Professeur-Camille-Soula, 31400 Toulouse, France

Available online 21 July 2009

Abstract

Large-Eddy Simulations (LES) of an evaporating two-phase flow in an experimental burner are performed using two different solvers, CDP from CTR-Stanford and AVBP from CERFACS, on the same grid and for the same operating conditions. Results are evaluated by comparison with experimental data. The CDP code uses a Lagrangian particle tracking method (EL) while the code AVBP can be coupled either with a mesoscopic Eulerian approach (EE) or with a Lagrangian method (EL). After a validation of the purely gaseous flow in the burner, liquid-phase dynamics, droplet dispersion and fuel evaporation are qualitatively and quantitatively evaluated for three two-phase flow simulations. They are respectively referred as: CDP-EL, AVBP-EE and AVBP-EL. The results of the three simulations show reasonable agreement with experiments for the two-phase flow case. **To cite this article: J.M. Senoner et al., C. R. Mecanique 337 (2009).**

© 2009 Published by Elsevier Masson SAS on behalf of Académie des sciences.

Résumé

Simulations eulériennes et lagrangiennes aux grandes échelles d'un écoulement diphasique évaporant. Les simulations aux grandes échelles (SGE) de l'écoulement diphasique évaporant dans un brûleur expérimental sont réalisées avec deux codes numériques différents, CDP du CTR-Stanford et AVBP du CERFACS, sur le même maillage et pour les mêmes points de fonctionnement. Les résultats obtenus sont validés par comparaison avec des données expérimentales. Le code CDP peut être couplé à une méthode de suivi Lagrangien de la phase liquide (EL). Le code AVBP peut soit être couplé à une méthode mésoscopique Eulerienne (EE), soit à une méthode de suivi Lagrangien (EL). Après validation de l'écoulement purement gazeux dans le brûleur, la dynamique de la phase liquide, la dispersion et l'évaporation du carburant sont évaluées qualitativement et quantitativement pour trois simulations diphasiques dénotées respectivement : CDP-EL, AVBP-EE et AVBP-EL. Les résultats obtenus par les trois simulations sont en accord raisonnable avec l'expérience pour l'écoulement diphasique. **Pour citer cet article : J.M. Senoner et al., C. R. Mecanique 337 (2009).**

© 2009 Published by Elsevier Masson SAS on behalf of Académie des sciences.

Keywords: Combustion; Two-phase flows; Eulerian; Lagrangian; Large-Eddy Simulation

Mots-clés : Combustion ; Écoulements diphasiques ; Eulérien ; Lagrangien ; Simulation aux grandes échelles

* Corresponding author.

E-mail address: senoner@cerfacs.fr (J.M. Senoner).

1. Introduction

Large-Eddy Simulation (LES) is becoming a standard tool for combustion system analysis since it has extensively demonstrated its ability to predict mean and unsteady reactive gaseous flows in complex geometries [1,2]. Therefore, LES seems a natural candidate for the investigation of the complex physical phenomena involved in reacting two-phase flows, for which two numerical strategies can be applied:

- In Euler–Lagrange (EL) simulations, the gas is modelled by a classical Eulerian approach whereas particles are tracked in a Lagrangian framework [3,4];
- Euler–Euler (EE) simulations use the Eulerian description for the gaseous and the dispersed phases [5,6].

The Euler–Lagrange approach is commonly used as individual droplet physical mechanisms can be easily implemented: polydispersion of a spray, crossing trajectories, bouncing on walls, group and wake combustion of droplets. However, the large number of tracked particles in real applications and their localisation in the vicinity of the injector lead to load balancing issues since the droplets are only present on few processors. Thus, the Euler–Euler approach is sometimes preferred as the parallelisation of the liquid phase solver is identical to the gas solver. However, modelling aspects are generally more difficult to treat in the Euler–Euler framework.

A joint effort between CERFACS, CTR, ONERA and TURBOMECA led to the experimental and numerical investigation of the flow features in a swirl-stabilised lab burner, called MERCATO, fuelled with liquid Jet-A kerosene and operated at conditions where two-phase effects are significant.

In the present work the influence of time advancement and dispersed phase treatment are evaluated for a nonreacting evaporating flow as a first step to the simulation of reacting systems. Three LES's of the experiment are compared using both approaches: two simulations are based on the explicit fully compressible solver AVBP (respectively referred as AVBP-EL and AVBP-EE) in which both approaches are implemented, a third uses the implicit incompressible solver CDP from CTR-Stanford combined with a Lagrangian particle tracking technique (CDP-EL). Simulations are performed on the same grid for two regimes: (I) purely gaseous flow, (II) gaseous flow with evaporating droplets. Available experimental data for regimes I and II include mean and root-mean square (RMS) velocity fields for the gas and for the droplets.

The paper is organised as follows: Section 2 describes the MERCATO configuration and its operating conditions. Section 3 is devoted to the numerical methods. Finally, results are discussed for the two cases presented above in Section 4, followed by a conclusion.

2. Configuration

The experimental rig MERCATO (Fig. 1) is a swirled combustor fed with air and Jet-A liquid fuel. The plenum and combustion chamber have square sections of respectively 100 mm and 130 mm. They respectively measure 200 mm and 285 mm. The regimes considered are presented in Table 1. Case I is a purely gaseous flow. For Case II, the air is heated up to 463 K to enhance evaporation and reduce the formation of liquid fuel films on visualisation windows.

For Case I, LDA measurements were performed on the gas seeded with fine oil droplets ($<2\ \mu\text{m}$). The mean and root-mean-square (RMS) gas velocity fields were obtained in five axial planes ($z = 6\ \text{mm}$, $z = 26\ \text{mm}$, $z = 56\ \text{mm}$, $z = 86\ \text{mm}$, $z = 116\ \text{mm}$), z being the axial distance from the chamber inlet plane. For Case II, PDA measurements were performed to obtain the mean and RMS velocity fields of the droplets in three axial planes ($z = 6\ \text{mm}$, $z = 26\ \text{mm}$, $z = 56\ \text{mm}$).

3. Numerics

3.1. Gas phase

3.1.1. CDP gas solver

The LES code CDP implicitly solves the filtered incompressible Navier–Stokes equations. Time integration in CDP is based on the fractional-step method [7] and space integration relies on a second-order centred scheme which

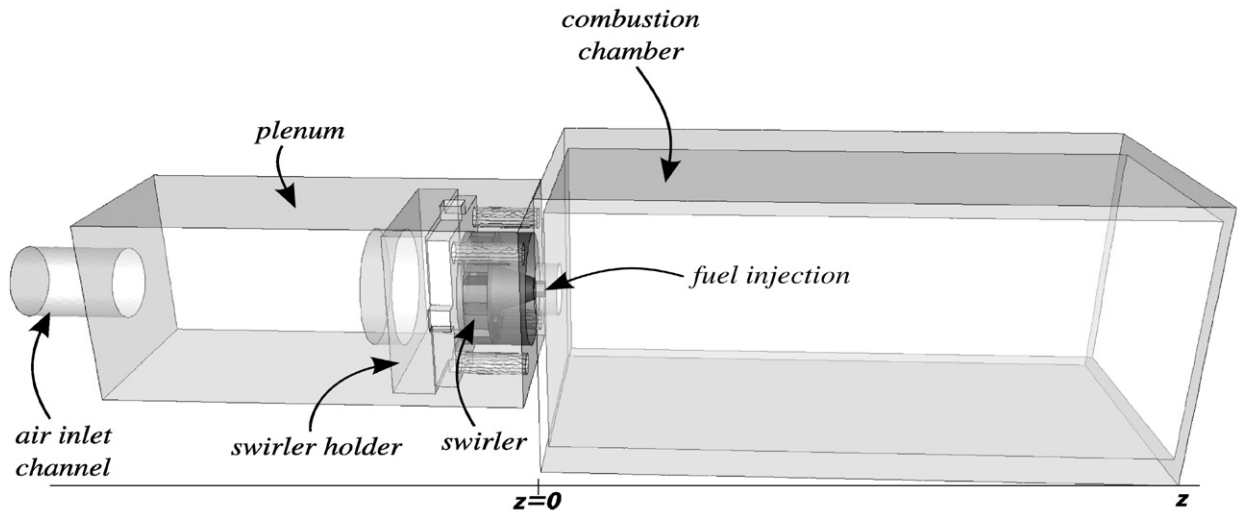


Fig. 1. The MERCATO configuration (ONERA Toulouse).

Table 1

Summary of operating points for the gaseous flow (Case I) and the two-phase flow (Case II).

Case	Pressure (atm)	Temperature (K)		Flow rate (g/s)		Equivalence ratio
		Liquid	Air	Air	Fuel	
I: gaseous flow	1	–	300	15	–	–
II: gaseous flow + droplets	1	300	463	15	1	1.0

conserves the kinetic energy while being free of numerical dissipation [8]. The dynamic Smagorinsky model [9] is used for closure of the subgrid stress tensor.

3.1.2. AVBP gas solver

The LES code AVBP explicitly solves the filtered compressible Navier–Stokes equations with a centred finite-element scheme which achieves third-order accuracy in both time and space [10]. The WALE model is used for closure of the subgrid stress tensor [11]. Boundary conditions treatment relies on the NSCBC formalism [12].

3.2. Equations for the dispersed liquid-phase

For both approaches, it is assumed that (1) the density of the droplets is much larger than that of the carrier fluid, (2) the droplets are dispersed and collisions between them are negligible, (3) the droplets are much smaller than the LES filter width, (4) droplet deformation effects are small, (5) motion due to shear is negligible and (6) gravitational effects are not significant compared to drag.

The governing equations of motion for the dispersed liquid-phase of both Euler–Lagrange and Euler–Euler formalisms are presented in the two next subsections. The evaporation models and the treatment of source terms are described in common subsections.

3.2.1. Euler–Lagrange approach

The Lagrangian equations governing the droplet motion are written:

$$\frac{dx_{p,i}}{dt} = u_{p,i} \quad (1)$$

and:

$$\frac{du_{p,i}}{dt} = \frac{1}{\tau_p} (\tilde{u}_{g@p,i} - u_{p,i}) \quad (2)$$

where $x_{p,i}$, ρ_p and ρ_g respectively denote the position of the droplet centroid, the liquid and gas-phase densities. $u_{p,i}$ is the droplet velocity and $\tilde{u}_{g@p,i}$ the resolved gas-phase velocity interpolated at the droplet location. The droplet relaxation timescale τ_p writes:

$$\tau_p = \frac{4 \rho_p}{3 \rho_g} \frac{d_p}{C_D(Re_p) |\tilde{u}_{g@p,i} - u_{p,i}|} \tag{3}$$

where $C_D(Re_p)$ is the local drag coefficient depending on the droplet Reynolds number Re_p [13].

The direct effect of subgrid-scale fluctuations on particle motion is neglected for both Lagrangian approaches. This seems acceptable for swirling separated flows with subgrid scale energy contents much smaller than those of the resolved scales [14].

When dealing with evaporating droplets, equations for the droplet mass and temperature must be solved:

$$\frac{dm_p}{dt} = -\frac{m_p}{\tau_m} \tag{4}$$

and

$$\frac{dT_p}{dt} = \frac{-1}{m_p C_{p,l}} \left(\Phi_g^c + \frac{m_p}{\tau_m} L_v(T_\zeta) \right) \tag{5}$$

where L_v is the latent heat of vaporisation, m_p the mass of the droplet, T_p its temperature, T_ζ the temperature at the droplet surface and $C_{p,l}$ the specific heat of the liquid. Assuming a spherical shape, the diameter of the droplet is obtained from its mass: $d_p = (6m_p/\pi\rho_l)^{1/3}$. Here, τ_m is the droplet lifetime scale, and Φ_g^c the conductive heat flux on the gaseous side at the droplet surface. The terms on the right-hand side of Eqs. (4) and (5) are described in Section 3.2.3.

In both CDP-EL and AVBP-EL, the interpolation of gaseous properties to the droplet is based on a least-squares operator. For time advancement, CDP-EL uses a third order Runge–Kutta time stepping method while AVBP-EL relies on a first order method. The respective accuracies are consistent with the timesteps of the gaseous solvers, respectively the convective CFL for CDP (implicit scheme) and the acoustic CFL for AVBP (explicit scheme).

3.2.2. Euler–Euler approach

The Eulerian approach assumes that the dispersed phase can be described by a finite number of continuous properties which correspond to a conditional ensemble average of the droplet properties for a given gas-phase realisation. They are called the mesoscopic liquid properties. The monodisperse equation system used in this study is a simplification of the model by Février et al. [5]. It does not take into account the random uncorrelated motion [15]. The resulting model leads to equations for the droplet number density, the liquid volume fraction, the mesoscopic velocity and the mesoscopic enthalpy. By analogy to the gas-phase Favre filtering, a LES filter is applied to the mesoscopic equations $\tilde{\alpha}_l \hat{f}_l = \bar{\alpha}_l \hat{f}_l$ where $\bar{\alpha}_l$ is the spatially filtered liquid volume fraction. The final set of equations for the dispersed phase is summarised below. The drag-force is written $F_{d,i}$, with τ_p defined by Eq. (3). The evaporation rate is denoted Γ . The liquid phase convective and conductive heat mass transfers Φ_g^c and Φ_g^{ev} are gathered in Π . Details on the source terms are provided in Section 3.2.4.

$$\frac{\partial \bar{n}_l}{\partial t} + \frac{\partial \bar{n}_l \hat{u}_{l,j}}{\partial x_j} = 0 \tag{6}$$

$$\frac{\partial \rho_l \bar{\alpha}_l}{\partial t} + \frac{\partial \rho_l \bar{\alpha}_l \hat{u}_{l,j}}{\partial x_j} = -\Gamma \tag{7}$$

$$\frac{\partial \rho_l \bar{\alpha}_l \hat{u}_{l,i}}{\partial t} + \frac{\partial \rho_l \bar{\alpha}_l \hat{u}_{l,i} \hat{u}_{l,j}}{\partial x_j} = \rho_l \bar{\alpha}_l F_{d,i} - \hat{u}_{l,i} \Gamma + \frac{\partial \bar{\tau}_{l,ij}^f}{\partial x_j} \tag{8}$$

$$\frac{\partial \rho_l \bar{\alpha}_l \hat{h}_l}{\partial t} + \frac{\partial \rho_l \bar{\alpha}_l \hat{u}_{l,j} \hat{h}_l}{\partial x_j} = -\Pi \tag{9}$$

By analogy to compressible single-phase flows, the particle subgrid stress tensor $\bar{\tau}_{l,ij}^f$ is modelled using a Smagorinsky formulation for the trace-free part together with a Yoshizawa formulation for the trace part [16].

In the Euler–Euler approach, the same scheme as for the gaseous phase is used to solve the set of equations defined above. No interpolation procedure is involved for interphase exchange terms since for both phases quantities are available at the nodes of the mesh.

3.2.3. Evaporation models

The evaporation models of the three approaches assume infinite thermal conductivity of the liquid: the evaporation rate is driven by the thermal and species diffusion from the droplet surface into the gas phase. The surface droplet temperature is then equal to the constant droplet temperature $T_\zeta = T_p$. In the EE approach, the surface droplet temperature corresponds to the resolved mesoscopic temperature $T_\zeta \equiv \hat{T}_l$.

In the AVBP-EL and AVBP-EE solvers, the Nusselt (Nu) and Sherwood (Sh) numbers are modified following the Ranz–Marshall correlations [17] to take into account the effect of non-zero slip velocity between droplet and carrier phase. In the CDP-EL solver, this effect is modelled by the multiplicative correction for heat and mass transfer [18].

The liquid/gas interface is assumed to be in thermodynamic equilibrium, the Clausius–Clapeyron equilibrium vapour pressure relationship is used to compute the fuel mass fraction at the droplet surface.

This leads to the following expressions for the droplet lifetime τ_m and the convective heating time scales:

$$\frac{m_p}{\tau_m} = \pi d_p [\rho_g \mathcal{D}_F]^s \ln(1 + B) Sh \quad (10)$$

$$\Phi_g^c = \pi d_p Nu \lambda^s (T_\zeta - \tilde{T}_{g@p}) \frac{\ln(1 + B)}{B} \quad (11)$$

$$\Phi_g^{ev} = \frac{m_p}{\tau_m} h_{s,F}(T_\zeta) \quad (12)$$

The latent heat of vapourisation is defined as the difference between the droplet enthalpy and the enthalpy of the fuel vapour, at the same temperature: $L_v(T_\zeta) = h_{s,F}(T_\zeta) - m_p C_{p,l} T_\zeta$. B stands for the Spalding number [19]. \mathcal{D}_F and λ are the fuel vapour diffusivity and conductivity, respectively. The superscript s stands for values considered constant throughout the gas layer around the droplets. To take into account the variation of composition and temperature of the gas between the droplet surface and the far-field, the gas properties are evaluated using the 1/3rd–2/3rd rule [20].

3.2.4. Source terms

In the Euler–Euler approach, the source terms at a given node n correspond to a statistical mean over the realisations, written $\{\cdot\}_l$:

$$\Gamma_n = \bar{n}_l \left\{ -\frac{m_p}{\tau_m} \right\}_l \quad (13)$$

$$\Pi_n = \bar{n}_l \{ \Phi_g^c + \Phi_g^{ev} \}_l \quad (14)$$

In the Euler–Lagrange approach, the source terms of a particle p with coordinates $x_{p,i}$ are distributed among the nodes n of the cell K_e where this particle is located. The conservative weights $w_{p@n}$ are calculated as follows:

$$w_{p@n} = \frac{\prod_{j \neq n} |x_{p,i} - x_{j,i}|}{\sum_{k \in K_e} \prod_{l \neq k} |x_{p,i} - x_{l,i}|} \quad \text{for } n \in K_e \quad (15)$$

with $x_{n,i}$ the coordinates of the nodes, and $|\cdot|$ the norm operator. Summing over all particles M located in one of the cells sharing the node n , one obtains:

$$\Gamma_n = \sum_{p=1}^M w_{p@n} \left(-\frac{m_p}{\tau_m} \right) \quad (16)$$

$$\Pi_n = \sum_{p=1}^M w_{p@n} (\Phi_g^c + \Phi_g^{ev}) \quad (17)$$

Table 2
Summary of surrogate fuel properties used.

Solver surrogate reference	Composition (in volume)	Molar weight (g/mol)	Boiling temperature (K@1 atm)
CDP-EL	80% of <i>n</i> -decane 20% tri-methyl-benzene	165	606.5
AVBP-EE and AVBP-EL [21]	74% of <i>n</i> -decane 15% propyl-benzene 11% propyl-cyclo-hexane	137.2	445.1

3.3. Choice of a surrogate for kerosene

Jet-A is a mixture of a large number of hydrocarbons and additives. In the LES's, kerosene is modelled by a single *meta* species built as an average of the thermodynamic properties of the multi-component surrogates. Two different surrogates are used for the CDP-EL simulation and the AVBP-EL/AVBP-EE simulations. For both surrogates, the liquid density is 781 kg/m³, the heat of vaporisation is around 3×10^5 J/kg, the liquid heat capacity is around 2×10^3 J/kg/K. Table 2 summarises the differences in molar weight and boiling temperature for both surrogates.

3.4. Liquid boundary conditions

In the CDP-EL simulations, particles are elastically bouncing at walls while no treatment is applied in the AVBP-EL simulations. In the AVBP-EE simulation the liquid phase fulfils a slip condition at walls. One of the main factors controlling the dispersion of the droplets is the description of the injection pattern. In this study there is no computation of the atomisation process at the injector outlet and the three approaches have to rely on measurements and empirical correlations to specify the injection condition on the atomiser outlet plane. The liquid injection boundary conditions are based on a methodology which specifies tangential and axial outflow velocity components following the empirical correlations of Rizk and Lefebvre [22]. Inlet profiles are reconstructed without parameter adjustment from the following quantities: the liquid flow rate, the spray angle and the orifice diameter. These inlet profiles are used in the CDP-EL simulation. In AVBP-EE the discharge orifice of the atomiser (diameter 0.5 mm) must be sufficiently meshed to control the flow rate through the boundary. A compromise between discretising the boundary patch and keeping a reasonable time step (limited by the smallest cell in the domain) is found in enlarging the boundary condition area which is translated a few millimetres downstream from the real injection position. Boundary profiles are built from the inlet empirical profiles (also used in CDP-EL) and applying the air entrainment model of Cossali [23].

In the AVBP-EL approach, particles are injected from a discrete point corresponding to the real injector position while the same empirical correlations as in the AVBP-EE/CDP-EL approaches are used to determine particle velocities. Particles are injected with a random angle ranging between zero and the experimentally specified spray angle (40°). The axial velocity is constant while the tangential velocity component is a linear function of the injection angle. No RMS value is specified at injection. For both AVBP-EL and CDP-EL, the initial droplet diameter is sampled from a Lognormal distribution fitted with the spatially averaged experimental probability density function (pdf) of droplet diameters at the first measurement plane ($z = 6$ mm). For the AVBP-EE simulation the first moment of the distribution is used for injection.

4. Results

4.1. Gas flow without droplets (Case I)

Figs. 2 and 3 show mean and RMS gas velocity profiles in the axial and transverse direction for five axial positions. The results of two AVBP and CDP gaseous simulations are compared with the experimental data (symbols). The averaging time in both LES codes is of the order of 400 ms, corresponding to approximately 10 flow-through times.

Both solvers capture the flow correctly and results are in very good agreement with experiments. Some discrepancies with experiments may be observed for the mean axial and tangential velocities, Figs. 2 and 3, left, at the two last stations. However, measurement uncertainties are expected to be large in this low speed region as the experimental

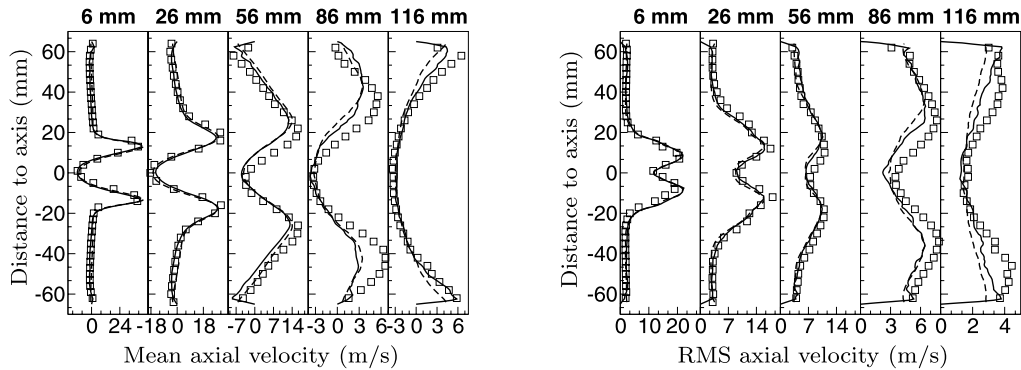


Fig. 2. Gaseous axial velocity (Case I). Left: mean, right: RMS. \square LDA, — CDP, -- AVBP.

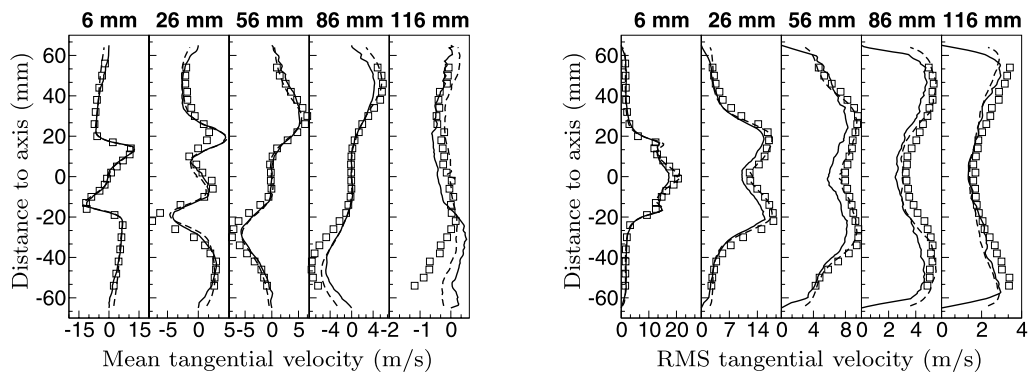


Fig. 3. Gaseous tangential velocity (Case I). Left: mean, right: RMS. \square LDA, — CDP, -- AVBP.

profiles are not symmetric. Slight differences between the two codes appear especially for RMS of tangential velocity, see Fig. 3, right. Here, the higher order of spatial accuracy of AVBP seems to provide a better representation of the unsteady flowfield. On the other hand, the lower numerical dissipation of CDP can be noticed in the last measurement plane for all velocity profiles as they lie above those of AVBP.

4.2. Gas flow with evaporating droplets (Case II)

For Case II, droplets are injected starting from a well-established gas-phase solution. Figs. 4 and 5a show an instantaneous view of droplet distribution in the combustion chamber. The three simulations capture the main structures of droplet preferential concentration: the central recirculation zone has a low droplet density, dense pockets of droplets can be seen in the shear layer of the swirled-air jet and droplets are trapped in the recirculation zone in corners of the chamber. Such droplet concentrations lead to fuel vapour inhomogeneities through the evaporation source terms, as shown in Figs. 5b and 6. In the CDP-EL simulation, the liquid seems to evaporate more strongly close to the injector exit, as indicated by the evaporation rate isocontours (3 levels of respectively 7, 14 and 21 kg/m³/s). Such high evaporation rates are not observed in the AVBP-EL simulation which injects the same polydisperse spray. Thus, differences seem rather to be caused by the different surrogate or the evaporation model than by the evaporation of small droplets.

The droplet velocity profiles at four axial planes are compared in Figs. 7, 8. The first plane ($z = 0$ mm) is not an experimental measurement plane but is added for comparison of the profiles very close to the injector ($z = -3$ mm). Only averaged velocities (over all droplet size classes) are shown as the EE approach only resolves a monodisperse spray. The averaging time in the three simulations is of the order of 80 ms, corresponding to approximately 2 flow-through times. The CDP-EL statistics are not properly converged in areas where the droplets density is low, such as the chamber centreline. It is surprising to note that the AVBP-EL simulations display far better statistical convergence,

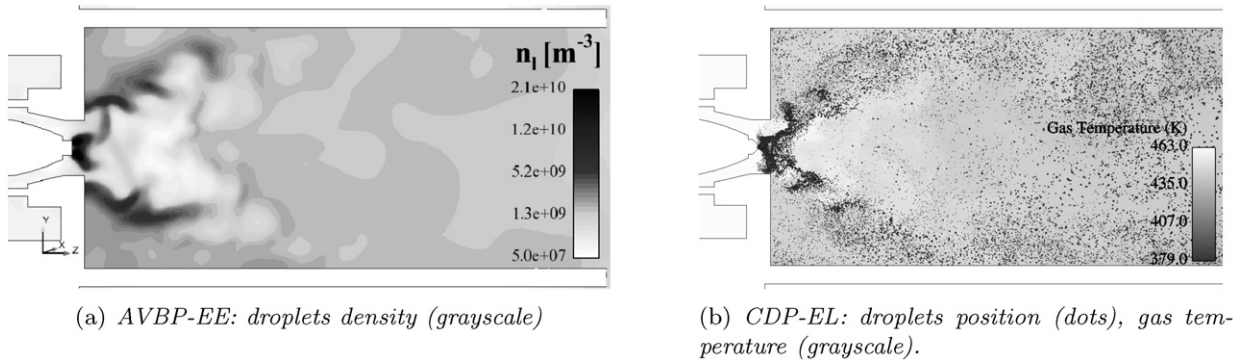


Fig. 4. Instantaneous droplet distribution in the MERCATO chamber (Case II). Comparison between AVBP-EE and CDP-EL.

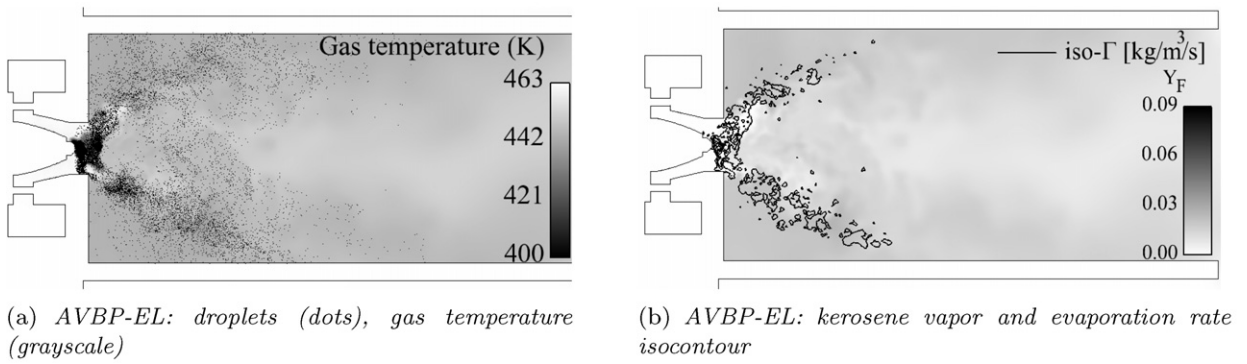


Fig. 5. AVBP-EL: Instantaneous droplet distribution in the MERCATO chamber and instantaneous kerosene vapour mass fraction with isocontours of evaporation rate (Case II).

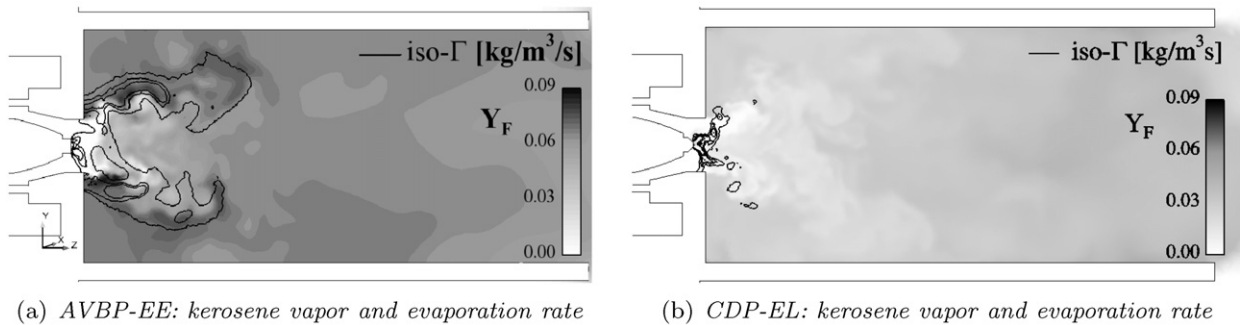


Fig. 6. Instantaneous kerosene vapour mass fraction (grayscale) and evaporation rate (isocontours).

maybe a consequence of the much smaller timestep of AVBP compared to CDP. The EE method clearly takes advantage of its continuous mesoscopic approach (transported quantities are averaged over the particle realisations) and results show the most converged profiles.

Note that the air flow rate was increased when performing the droplet LDA measurements at $z = 56$ mm to delay spray impingement on measurement windows. Thus, the comparisons between LES and experiments at this location are affected with larger uncertainties.

The agreement between the three simulations and the experimental profiles is good at $z = 6$ mm for the droplet axial and tangential velocities, showing that the injection procedures described in Section 3.4 are reasonable for such flows, where drag effects on particles are very pronounced. The agreement is still satisfying at $z = 26$ and 56 mm for axial velocity. Differences may be observed for all three simulations close to the axis where the recirculation zone is located. There, spatial segregation effects according to droplet size are expected to be significant. However,

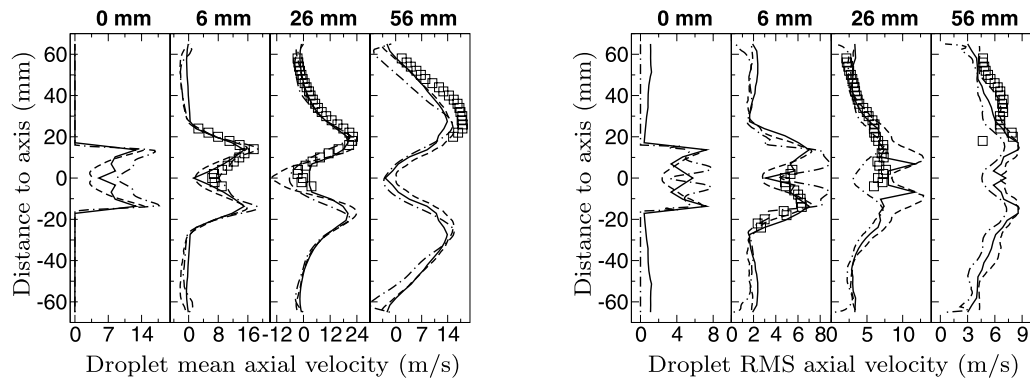


Fig. 7. Droplet axial velocity (Case II). Left: mean, right: RMS. \square PDA, — CDP-EL, -- AVBP-EL, -·- AVBP-EE.

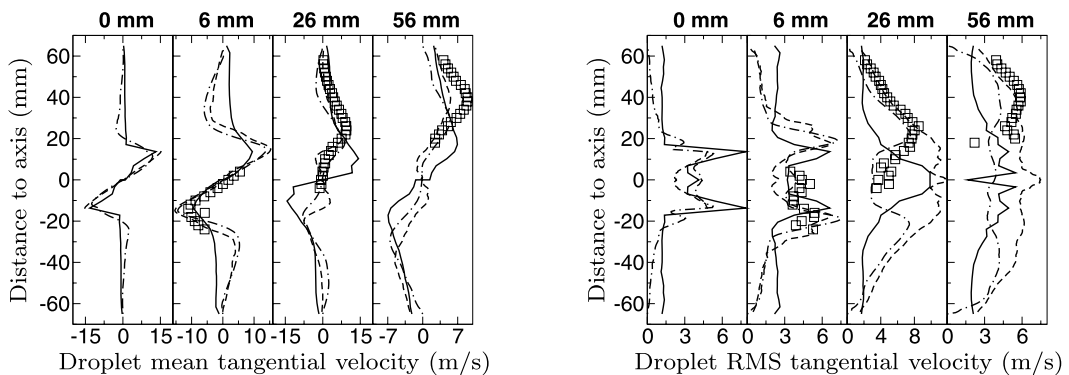


Fig. 8. Droplet tangential velocity (Case II). Left: mean, right: RMS. \square PDA, — CDP-EL, -- AVBP-EL, -·- AVBP-EE.

the polydisperse Lagrangian simulations do not provide more accurate results in this zone than the monodisperse Eulerian simulation. The three simulations fail to reproduce the shape and the levels of axial RMS velocity at the first location. For the next stations, the three simulations reproduce the right fluctuation levels, but the shapes of the profiles are not well captured, even though the experimental data is quite noisy.

Concerning the mean tangential component shown in Fig. 8, the three simulations predict the right opening of the spray at $z = 6$ mm, but the discrepancies increase as the spray goes downstream. The maximum value and location are not well predicted at $z = 26$ mm and $z = 56$ mm. The polydisperse AVBP-EL and monodisperse AVBP-EE results are very close at $z = 6$ mm and the increasing differences between them $z = 26$ mm and $z = 56$ mm may originate from polydisperse effects. However, results do not significantly improve for AVBP-EL. Looking at the RMS values of the droplets tangential component shown in Fig. 8, the shape and values are well reproduced by the AVBP-EE simulation while the AVBP-EL simulation fails to predict the decrease close to the centreline at $z = 26$ mm. The CDP-EL statistics of this component are not sufficiently converged to compare them with experiments.

4.3. Comparison of computational cost

Table 3 gives a comparison of the computational times for the AVBP-EE and AVBP-EL simulations on different numbers of processors. All parameters are identical for the gaseous phase and initialisation time is negligible in comparison with computational time. The AVBP-EL calculation is performed with 285 000 droplets, no dynamical load balancing is performed.

The AVBP-EL solver is nearly twice as fast as the AVBP-EE solver, demonstrating that the Lagrangian particle tracking method is well suited for low particle numbers. However, AVBP-EE closely follows the ideal speed-up curve whereas AVBP-EL suffers from the absence of dynamical load balancing. Moreover, it must be remembered that the computational cost of AVBP-EE is independent of particle number.

Table 3

Comparison of reduced efficiencies on an IBM Blue Gene/L supercomputer. The reduced efficiency is the CPU time per mesh node and per iteration ($\mu\text{s}/\text{iteration}/\text{node}$).

Processor numbers	256	1024
AVBP-EE	4.342	1.154
AVBP-EL	2.842	0.874

5. Conclusions

The precision of two LES solvers (AVBP/CDP) combined with two different approaches for the modelling of the dispersed phase (Eulerian/Lagrangian) has been compared in the case of a swirled liquid kerosene/air combustor experimentally investigated at ONERA Toulouse. The agreement with experiments for the gaseous phase is very good for both LES solvers. For the dispersed phase, mean axial velocity profiles are correctly reproduced while the opening of the spray is mispredicted further downstream. Moreover, only correct fluctuation levels are obtained for RMS velocity profiles. Finally, a clear gain of accuracy could not be evidenced for the polydisperse Lagrangian simulations compared to the monodisperse Eulerian simulation. This may be a consequence of the simplified injection model and requires further investigation.

Acknowledgements

The supports of TURBOMECA, of the Délégation générale de l'armement, of the Center of Turbulence Research (Stanford), of the European Community through the TIMECOP-AE project (#AST-CT-2006-030828) and Marie Curie Fellowships (contract MEST-CT-2005-020426) are gratefully acknowledged.

References

- [1] H. El-Asrag, S. Menon, Large eddy simulation of bluff-body stabilized swirling non-premixed flames, *Proceedings of the Combustion Institute* 31 (2007) 1747–1754.
- [2] C. Duwig, C. Fureby, Large eddy simulation of unsteady lean stratified premixed combustion, *Combustion and Flame* 151 (1–2) (2007) 85–103.
- [3] K. Mahesh, G. Constantinescu, S. Apte, G. Iaccarino, F. Ham, P. Moin, Large eddy simulation of reacting turbulent flows in complex geometries, *ASME Journal of the Applied Mechanics* 73 (2006) 374–381.
- [4] N. Patel, S. Menon, Simulation of spray–turbulence–flame interactions in a lean direct injection combustor, *Combustion and Flame* 153 (1–2) (2008) 228–257.
- [5] P. Février, O. Simonin, K. Squires, Partitioning of particle velocities in gas–solid turbulent flows into a continuous field and a spatially uncorrelated random distribution: Theoretical formalism and numerical study, *Journal of Fluid Mechanics* 533 (2005) 1–46.
- [6] M. Boileau, S. Pascaud, E. Riber, B. Cuenot, L.Y.M. Gicquel, T. Poinsot, M. Cazalens, Investigation of two-fluid methods for Large Eddy Simulation of spray combustion in gas turbines, *Flow, Turbulence and Combustion* 80 (3) (2008) 291–321.
- [7] J. Kim, P. Moin, Application of a fractional-step method to incompressible Navier–Stokes equations, *Journal of Computational Physics* 59 (2) (1985) 308–323.
- [8] K. Mahesh, G. Constantinescu, P. Moin, A numerical method for large-eddy simulation in complex geometries, *Journal of Computational Physics* 197 (1) (2004) 215–240.
- [9] M. Germano, U. Piomelli, P. Moin, W. Cabot, A dynamic subgrid-scale eddy viscosity model, *Physics of Fluids* 3 (7) (1991) 1760–1765.
- [10] O. Colin, M. Rudyard, Development of high-order Taylor–Galerkin schemes for unsteady calculations, *Journal of Computational Physics* 162 (2) (2000) 338–371.
- [11] F. Nicoud, F. Ducros, Subgrid-scale stress modelling based on the square of the velocity gradient, *Flow, Turbulence and Combustion* 62 (3) (1999) 183–200.
- [12] V. Moureau, G. Lartigue, Y. Sommerer, C. Angelberger, O. Colin, T. Poinsot, High-order methods for DNS and LES of compressible multi-component reacting flows on fixed and moving grids, *Journal of Computational Physics* 202 (2) (2005) 710–736.
- [13] L. Schiller, A. Nauman, A drag coefficient correlation, *VDI Zeitung* 77 (1935) 318–320.
- [14] S.V. Apte, K.P. Mahesh, P. Moin, J.C. Oefelein, Large-eddy simulation of swirling particle-laden flows in a coaxial-jet combustor, *International Journal of Multiphase Flow* 29 (2003) 1311–1331.
- [15] E. Riber, V. Moureau, M. García, T. Poinsot, O. Simonin, Evaluation of numerical strategies for LES of particulate two-phase recirculating flows, *Journal of Computational Physics* 228 (2009) 539–564.
- [16] M. Moreau, Modélisation numérique directe et des grandes échelles des écoulements turbulents gaz-particules dans le formalisme eulérien mésoscopique, Ph.D. thesis, INP Toulouse, 2006.
- [17] W.E. Ranz, W.R. Marshall, Evaporation from drops, *Chemical Engineering Progress* 48 (4) (1952) 173.

- [18] G.M. Faeth, Evaporation and combustion of sprays, *Progress in Energy and Combustion Science* 9 (1983) 1–76.
- [19] K.K. Kuo, *Principles of Combustion*, John Wiley, New York, 1986.
- [20] G.L. Hubbard, V.E. Denny, A.F. Mills, Droplet evaporation: Effects of transient and variable properties, *International Journal of Heat and Mass Transfer* 18 (1975) 1003–1008.
- [21] J. Luche, Elaboration of reduced kinetic models of combustion. Application to a kerosene mechanism, Ph.D. thesis, LCSR Orleans, 2003.
- [22] N.K. Rizk, A.H. Lefebvre, Internal flow characteristics of simplex atomizer, *Journal of Propulsion and Power* 1 (3) (May–June 1985) 193–199.
- [23] G.E. Cossali, An integral model for gas entrainment into full cone sprays, *Journal of Fluid Mechanics* 439 (2001) 353–366.